THE EUROPEAN
PHYSICAL JOURNAL A

Understanding the energy dependence of B_2 in heavy ion collisions: interplay of volume and space-momentum correlations

Vincent Gaebel[1,a] , **Michel Bonne**[1], **Tom Reichert**[1], **Ajdin Burnic**[5], **Paula Hillmann**[1,2,3,4], **Marcus Bleicher**[1,2,3,4]

[1] Institut für Theoretische Physik, Goethe Universität Frankfurt, Max-von-Laue-Strasse 1, 60438 Frankfurt am Main, Germany

[2] GSI Helmholtzzentrum für Schwerionenforschung GmbH, Planckstr. 1, Darmstadt 64291, Germany

[3] John von Neumann-Institut für Computing, Forschungzentrum Jülich, 52425 Jülich, Germany

[4] Helmholtz Research Academy Hesse for FAIR, Campus Frankfurt, Frankfurt, Germany

[5] University of Sarajevo, Sarajevo, Bosnia and Herzegovina

Abstract The deuteron coalescence parameter B_2 in proton+proton and nucleus+nucleus collisions in the energy range of $\sqrt{s_{NN}} = 900$–7000 GeV for proton + proton and $\sqrt{s_{NN}} = 2$–2760 GeV for nucleus + nucleus collisions is analyzed with the Ultrarelativistic Quantum Molecular Dynamics (UrQMD) transport model, supplemented by an event-by-event phase space coalescence model for deuteron and antideuteron production. The results are compared to data by the E866, E877, PHENIX, STAR and ALICE experiments. The B_2 values are calculated from the final spectra of protons and deuterons. At lower energies, $\sqrt{s_{NN}} \leq 20$ GeV, B_2 drops drastically with increasing energy. The calculations confirm that this is due to the increasing freeze-out volume reflected in $B_2 \sim 1/V$. At higher energies, $\sqrt{s_{NN}} \geq 20$ GeV, B_2 saturates at a constant level. This qualitative change and the vanishing of the volume suppression is shown to be due to the development of strong radial flow with increasing energy. The flow leads to strong space-momentum correlations which counteract the volume effect.

1 Introduction

The exploration of the theory of strong interaction, called Quantum Chromodynamics (QCD), is one of the major goals of today's high energy physics. QCD is a non-abelian gauge theory that predicts a transition of the known hadronic matter seen in nuclei at ground-state density to a fluid-like state called the Quark-Gluon-Plasma, QGP. This transition may either happen if a critical temperature around 150–160 MeV is reached or if a critical baryon density, around 4-5 times the ground state density, is created [1]. Naturally, this state appeared a few nanoseconds after the Big Bang and is currently present in compact stellar objects like Neutron Stars. Understanding the QGP and its features is one of the key tasks of today's research in nuclear physics. Heavy ion collisions are therefore carried out and investigated in particle accelerators and colliders at CERN, BNL, GSI and NICA.

The study of cluster formation processes in heavy ion collisions is of particular interest for a multitude of reasons: Firstly, clusters probe the two-particle baryon correlations in phase space, i.e. they allow to explore the space and momentum space structure of the emission source [2]. Secondly, the production rate might allow to distinguish thermal production from coalescence [3]. Thirdly, clusters, e.g. anti-matter, (multi-)strange objects like the hyper tritons, or even charmed clusters are themselves the objects of study and can be produced in hadronic collisions [4–6].

As a first step to classify the production process, this paper investigates the formation of deuterons by the phase space coalescence of protons and neutrons. The phase space coalescence model has been shown to provide a good theoretical description of the formation of clusters in the considered energy ranges [7–11]. The idea behind the coalescence model is that if a proton and a neutron are close enough in (momentum) space they can form a deuteron [12–15].

In the coalescence picture, the probability of creating N_d deuterons in a certain momentum space volume after freeze-out is proportional to the number of produced neutrons N_n and protons N_p (which can be further simplified, if one assumes the same number of protons and neutrons) [16]:

$$N_d \sim N_n \cdot N_p \sim N_p^2 \tag{1}$$

a e-mail: gaebel@itp.uni-frankfurt.de (corresponding author)

Springer

Assuming, e.g. a thermal system and the same yield of protons and neutrons, we have $N_d \sim V$, $N_p \sim V$, and therefore $N_d/N_p^2 \sim B_2 \sim 1/V$. In this context, B_2 is called the coalescence parameter for deuteron production. I.e., the measurable quantity B_2 encodes information on the inaccessible spatial extent of the source. It is also clear that, in general, such a result might be modified by the details of the emitting source [17,18], correlations like flow and the internal wave function of the considered cluster [19].

2 The UrQMD model and coalescence

For the theoretical investigation of the collisions, we perform simulations using the Ultrarelativistic Quantum Molecular Dynamics (UrQMD) transport model in version 3.4 [20,21]. This model has a well established history for the description of hadron yields and spectra over a broad range of energies (see e.g. [22–27]).

2.1 The model

UrQMD is based on the covariant propagation of hadrons and their interactions by potentials and/or elastic and inelastic cross sections. UrQMD is either run in Boltzmann mode, i.e. it provides an effective solution to the relativistic Boltzmann equation or in the Hydro-Boltzmann hybrid mode (here abbreviated as "UrQMD + hydro"). In hybrid mode, during the most dense phase of the reaction, the Boltzmann equation is replaced by an (ideal) fluid-dynamical evolution of the hot and dense QCD matter [28–30]. In this mode, a phase transition to the QGP can be incorporated and compared to a purely hadronic treatment as well.

The evolution equations in the hybrid mode are then

$$\partial_\mu T^{\mu\nu} = 0, \qquad (2)$$
$$\partial_\mu j_N^\mu = 0, \qquad (3)$$

with the energy-momentum tensor $T^{\mu\nu}$ and the baryon current j_N^μ [30]. The initial state generated by UrQMD provides the equal time initial conditions for $T^{\mu\nu}$ and j^μ. The hydrodynamic evolution is followed until the system reaches the freeze-out hyper-surface. There, we use a Cooper-Frye prescription to particlize [31] the hydrodynamic cells stochastically. The propagation of the hadrons then proceeds in Boltzmann mode until kinetic freeze-out.

2.2 Deuteron formation by coalescence

For each event, UrQMD provides the 4-coordinates and 4-momenta of each hadron on the decoupling or freeze-out surface. Here freeze-out is defined for each hadron individually as the last space-time point of strong interaction, i.e.

scattering or decay. A proton and a neutron are then assumed to form a deuteron if their distance in space and momentum space is sufficiently small. The details of the deuteron formation as implemented in UrQMD can be found in [9]. This method is used for both simulation modes, the Boltzmann mode and the hybrid mode with the intermediate hydrodynamic stage as described above. In the hybrid case, deuterons from the Cooper-Frye-hypersurface (direct thermal production) are not taken into account, but only those formed later by coalescence in the late hadronic freeze-out stage [32].

2.3 Coalescence parameter B_2

The coalescence parameter B_2 has been introduced in the simplified momentum space coalescence approach under the assumption that the volume can be trivially integrated out. In this approach one can connect the cluster distribution in momentum space to the distribution of the nucleons [15] via

$$E_A \frac{dN_A}{d^3 P_A} = B_A \left(E_p \frac{dN_p}{d^3 P_p} \right)^Z \left(E_n \frac{dN_n}{d^3 P_n} \right)^N \Bigg|_{P_p = P_n = P_A/A}. \qquad (4)$$

Here, Z is the proton number, N the number of neutrons and A the mass number of the nucleus. P_A is the momentum of the cluster and P_p (P_n) are the momenta of the protons (neutrons). Thus, the invariant momentum distribution of the cluster is proportional to the invariant momentum distributions of its constituents at the same momentum per particle. The coalescence factor is generally called B_A.

Applying this to deuteron production (A = 2, Z = 1, N = 1), and rewriting the invariant momentum distribution in terms of rapidity y and transverse momentum p_T, one obtains the following expression for B_2 as a function of the transverse momentum [34,35]:

$$B_2(p_T) = \frac{\frac{1}{2\pi} \frac{d^3 N_d}{p_T dp_T dy}\Big|_{p_T^d = 2 \cdot p_T^p}}{\left(\frac{1}{2\pi} \frac{d^3 N_p}{p_T dp_T dy} \right)^2}. \qquad (5)$$

This includes the assumption that the distribution is the same for protons and neutrons. Let us note that B_2 can be related (under certain assumptions) to the source size of the nucleons via [2]

$$R_G^3 = \frac{3}{4} \pi^{\frac{3}{2}} \frac{m_d}{m_p^2} B_2^{-1}, \qquad (6)$$

where R_G denotes the Gaussian radius of the source. Thus, the value of B_2 depends on the momentum distributions of the deuterons and the protons and indirectly encodes the spatial size of the proton source.
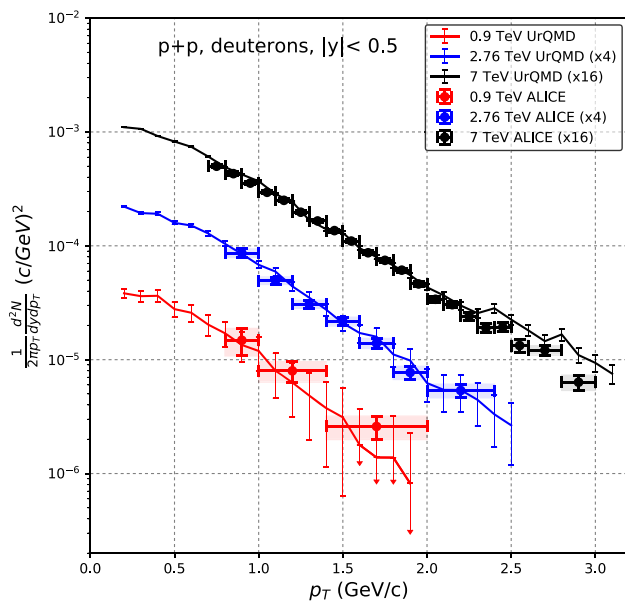
Fig. 1 Invariant deuteron yields at midrapidity as a function of the transverse momentum p_T in inelastic p + p collisions at different beam energies of $\sqrt{s_{NN}}$ = 0.9 TeV, 2.76 TeV and 7 TeV. The lines denote the UrQMD simulations and the circles the experimental data [33]
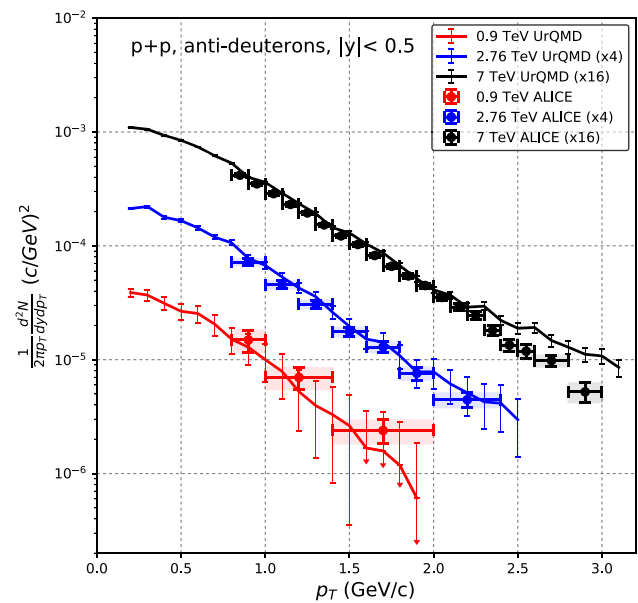

Fig. 2 Invariant anti-deuteron yields at midrapidity as a function of the transverse momentum p_T in inelastic p + p collisions at different beam energies of $\sqrt{s_{NN}}$ = 0.9 TeV, 2.76 TeV and 7 TeV. The lines denote the UrQMD simulations and the circles the experimental data [33]

3 Results

The following section presents comparisons of different experimental data (ALICE [33,36,37], STAR [38,39], E866 [39], E877 [39] and PHENIX [39]) to the simulation results from UrQMD.

3.1 Proton + proton reactions

Let us start with the exploration of proton + proton reactions in the TeV energy regime. Fig. 1 shows the invariant yield of deuterons as a function of transverse momentum in inelastic proton + proton collisions for three different energies $\sqrt{s_{NN}}$ = 0.9 TeV, 2.76 TeV and 7 TeV (bottom to top). The lines indicate the UrQMD simulations and the symbols the experimental data [33]. Generally, we observe a good description of the experimental data in the investigated energy regime. Nevertheless, in collisions at $\sqrt{s_{NN}}$ = 7 TeV towards higher transverse momenta, the simulation tends to deviate slightly from the data. For the proton spectra at the same collision energies we also observe an energy dependent overestimation of the data points at higher transverse momenta. This might indicate a slight overestimation of the jet cross section at high p_T in the model. The proton spectra can be tuned to the data using the Perugia SOFT tune [40] with CTEQ 5M1. After further testing, this tune will be implemented in the next version of UrQMD.

Next, we turn to the invariant transverse momentum distribution of the anti-deuterons for p + p collisions at different
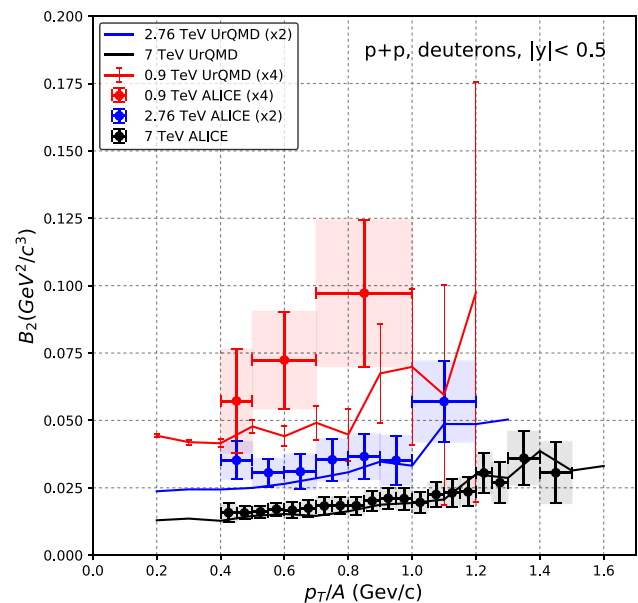

Fig. 3 B_2 against the transverse momentum scaled with the mass number (p_T/A) in inelastic p + p collisions at beam energies $\sqrt{s_{NN}}$ = 0.9 TeV, 2.76 TeV and 7 TeV. The lines denote the UrQMD simulations and the circles the experimental data [33]

beam energies of $\sqrt{s_{NN}}$ = 0.9 TeV, 2.76 TeV and 7 TeV (Fig. 2). The lines denote the UrQMD simulations and the circles the ALICE data points [33]. Again, we observe a good description of the data, with a slight deviation towards higher transverse momenta in $\sqrt{s_{NN}}$ = 7 TeV collisions.

To allow for a better interpretation of the data, we explore in Figs. 3 and 4 the coalescence parameter B_2 for deuterons
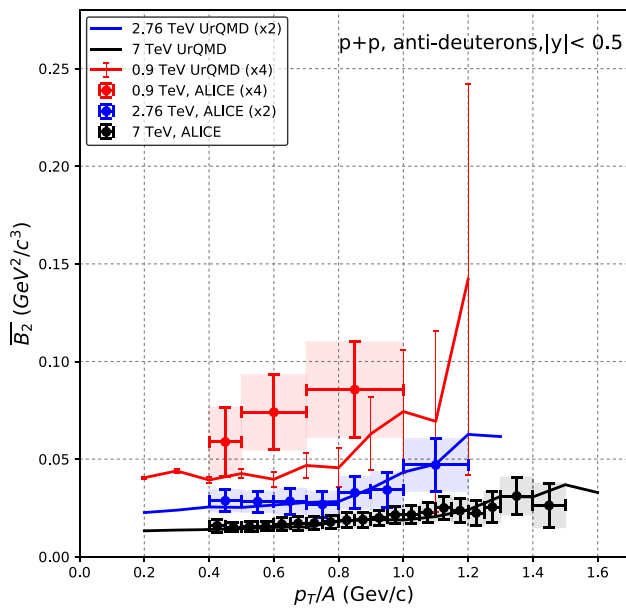
Fig. 4 $\bar{B}_2$ against the transverse momentum scaled with the mass number (p_T/A) in inelastic p + p collisions at beam energies $\sqrt{s_{NN}}$ = 0.9 TeV, 2.76 TeV and 7 TeV. The lines denote the UrQMD simulations and the circles the experimental data [33]
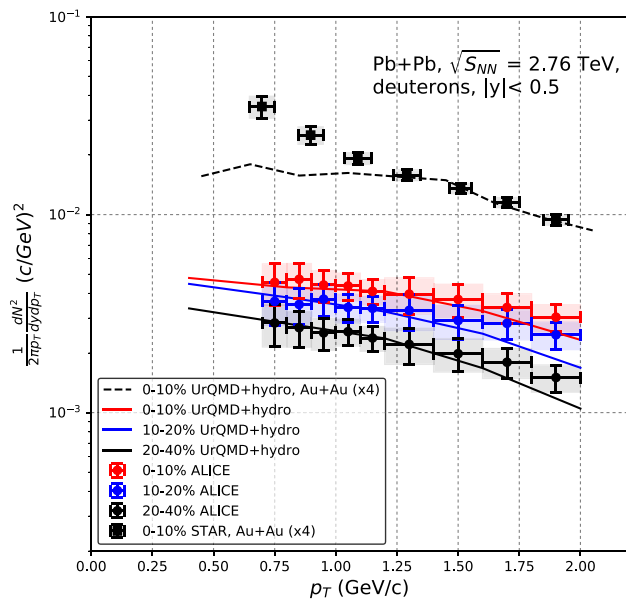

Fig. 5 Invariant transverse momentum distribution of deuterons for the 0–10%, 10–20% and 20–40% centrality classes in Pb + Pb collisions at $|y| < 0.5$ and $\sqrt{s_{NN}}$ = 2.76 TeV as well as for the 0–10% centraliy class in Au + Au reactions at $|y| < 0.3$ and $\sqrt{s_{NN}}$ = 200 GeV . The lines describe the UrQMD + hydro simulations and the symbols the ALICE and STAR data points [39,41]

and $\bar{B}_2$ for anti-deuterons in inelastic proton + proton reactions at the same energies as above (i.e. $\sqrt{s_{NN}}$ = 0.9 TeV, 2.76 TeV and 7 TeV). Again, the lines denote the UrQMD simulations and the circles the experimental data [33]. In both cases, the data at $\sqrt{s_{NN}}$ = 0.9 TeV show a strong increase of B_2 and $\bar{B}_2$ with increasing p_T/A. However, for
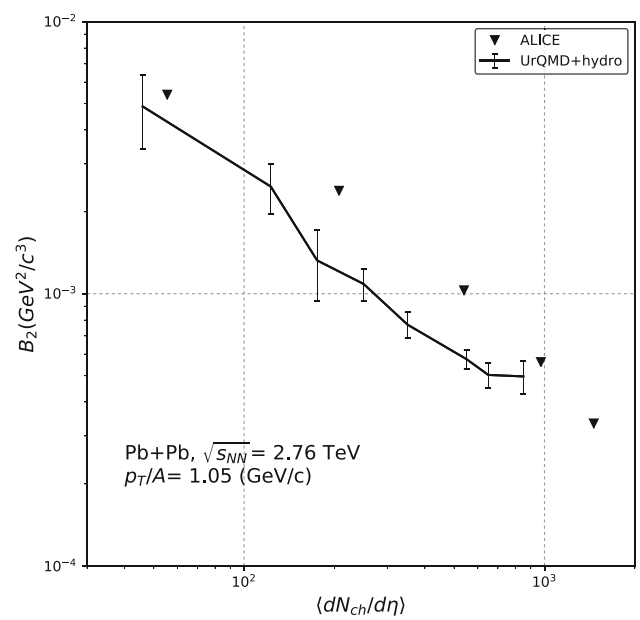

Fig. 6 B_2 as a function of the average charged-particle multiplicity in Pb + Pb collisions at fixed beam energy $\sqrt{s_{NN}}$ = 2.76 TeV at p_T/A = 1.05 GeV/c. The black line denotes the UrQMD + hydro simulations and the black triangles the ALICE data points [35]

both deuterons and anti-deuterons this increase is only very mildly observed for the two higher energies. The present model calculations show a good description of B_2 and $\bar{B}_2$ as a function of the transverse momentum at $\sqrt{s_{NN}}$ = 2.76 TeV and $\sqrt{s_{NN}}$ = 7 TeV. Although the calculations at $\sqrt{s_{NN}}$ = 0.9 TeV increase with p_T, the simulated results are below the data points.

Generally, (and in-line with standard HBT knowledge [2, 42]) the effectively observed source size decreases towards higher transverse momenta. This volume effect in the data of proton + proton collisions at top LHC energies is also consistent with previous model calculations [15].

3.2 Nucleus + nucleus reactions

Let us next turn to nucleus + nucleus collisions. Fig. 5 shows the invariant transverse momentum distribution of deuterons for three centrality classes (namely 0–10%, 10–20% and 20–40%) in Pb + Pb collisions at $\sqrt{s_{NN}}$ = 2.76 TeV. Additionally, the invariant deuteron yield for central Au + Au collisions (i.e. the 0–10% centrality bin) at $\sqrt{s_{NN}}$ = 200 GeV is presented. The lines describe the UrQMD + hydro simulations and the symbols the ALICE and STAR data points [39,41]. While the calculations for all centrality classes in Pb + Pb collisions match the data for low p_T values (p_T < 1.5 GeV/c) very well, we observe a deviation towards higher transverse momenta for all three curves.

In nucleus + nucleus collisions, the volume effect can be observed either in B_2's centrality dependence at fixed energy
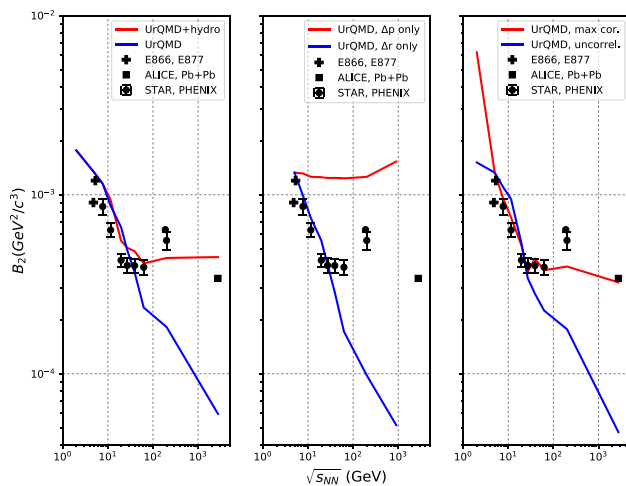
Fig. 7 B_2 at midrapidity and at $p_T/A = 0.65$ GeV/c as a function of the center-of-mass energy for central (0–10% centrality) Au + Au collisions. Additionally, the ALICE data point at $\sqrt{s_{NN}} = 2760$ GeV for central (0–10% centrality) Pb + Pb collisions is shown. The black symbols denote the data from different experiments (E866 [39], E877 [39], STAR [39], PHENIX [39], ALICE [35]). Left panel: the red line shows the UrQMD + hydro simulations and the blue line the UrQMD cascade calculations. Middle panel: the red line indicates the UrQMD B_2 values for simulations using only momentum space coalescence, while the blue line shows the simulation results using only space coalescence. Right panel: the red line denotes the UrQMD simulations with maximal space-momentum correlations and the blue line the uncorrelated UrQMD calculations

or in the energy dependence at fixed centrality. The centrality dependence of B_2 is exemplified in Fig. 6 for Pb + Pb reactions at $\sqrt{s_{NN}} = 2.76$ TeV. The black line denotes the UrQMD hybrid simulations and the black triangles the ALICE data points [12,37]. Here, the charged particle density encodes the centrality, i.e. larger particle densities correspond to larger volumes. This is clearly reflected in the multiplicity dependence of B_2 which strongly decreases with increasing charge particle number. While the trend of the data is described well and supports the volume suppression of deuteron formation, the B_2 values in the simulations are slightly lower than in the ALICE experiment.

In Fig. 7, we contrast the centrality dependence of B_2 with the energy dependence for central collisions. Fig. 7 shows B_2 at midrapidity and at $p_T/A = 0.65$ GeV/c as a function of the center-of-mass energy for central (0–10% centrality) Au + Au collisions. Additionally, the ALICE data point at $\sqrt{s_{NN}} = 2760$ GeV for central (0–10% centrality) Pb + Pb collisions is shown. The black symbols denote data from different experiments (E866 [39], E877 [39], STAR [39], PHENIX [39], ALICE [35]). The structure of the data can be summarized by a decrease of B_2 until $\sqrt{s_{NN}} = 20$ GeV, followed by a constant B_2 value at high energies. We will now try to understand this structure by various analyses:

(I) In the left panel of Fig. 7 we compare the data (symbols) to full UrQMD (blue line) and UrQMD +

hydro (red line) simulations. For both calculations, we perform full phase space coalescence using $\triangle p_{max} = 0.285$ GeV/c and $\triangle r_{max} = 3.575$ fm. One clearly observes that UrQMD + hydro with the full phase space coalescence approach is able to describe the data points nicely. Both regions, the strong decrease of B_2 and the constant level of B_2 above $\sqrt{s_{NN}} = 20$ GeV are described. In contrast, the UrQMD simulation without hydrodynamics can only capture the decrease of B_2.

(II) We analyze this behavior in Fig. 7 (middle). Here we show the data (symbols) in comparison to calculations using either only momentum space coalescence (red line), i.e. $\triangle p_{max} = 0.285$ GeV/c and $\triangle r_{max} = \infty$ or only space coalescence (blue line) using $\triangle p_{max} = \infty$ and $\triangle r_{max} = 3.575$ fm (both curves are normalized to the theoretical B_2 value at $\sqrt{s_{NN}} = 5$ GeV for better comparison). We clearly observe that the decrease until $\sqrt{s_{NN}} = 20$ GeV is driven by the volume of the source [43]. However, the flattening cannot be captured and the differences between the two UrQMD calculations cannot be explained.

(III) To pin down the origin of the flattening of the curve at higher energies, Fig. 7 finally compares the data (symbols) to UrQMD calculations with modified space-momentum correlations of the nucleons before coalescence. The idea is that for an expanding source the momentum **p** and the position **r** are correlated, if the transverse flow is sufficiently strong. For the correlation analysis, we compare a maximally space-momentum correlated nucleon source (constructed by enforcing **p**||**r**) (red line) with a totally space-momentum uncorrelated source, constructed by randomly exchanging the momenta of the nucleons at different positions (shown as blue line). Again, both curves are normalized to the B_2 value at $\sqrt{s_{NN}} = 5$ GeV for better comparison. One clearly observes that the uncorrelated nucleon source shows only a decrease, however, the correlated nucleon source shows the desired leveling-off and a plateau of B_2 with increasing energy.

Thus, we are led to the following conclusions: The volume effect dominates at low energies, leading to a decreasing B_2 value until $\sqrt{s_{NN}} = 20$ GeV. Above $\sqrt{s_{NN}} = 20$ GeV radial flow leads to substantial space-momentum correlations of the nucleons which result in a plateau of B_2 towards high energies. This also explains the difference between the UrQMD simulations with and without hydrodynamic stage, the main effect of the hydrodynamic stage is to produce sufficient flow to create the necessary space momentum correlations to capture the plateau structure of B_2. However, it is noticeable that the measured value at $\sqrt{s_{NN}} = 200$ GeV is slightly above the B_2 plateau, whereas the data point at $\sqrt{s_{NN}} = 2.76$ TeV is somewhat below our curve. It is out of the scope of this paper to explain why there seems to be a tension between the top RHIC data and the LHC data on B_2.

4 Summary

In the present paper, we employed the UrQMD model to explore deuteron and anti-deuteron production in proton + proton and nucleus + nucleus reactions in the RHIC-BES and LHC energy regime. To this aim, the UrQMD model was supplemented with a phase space coalescence approach to form deuterons. The analysis has focused on the coalescence parameter B_2 that has an intuitive physical interpretation suggesting $B_2 \sim 1/V$. For proton + proton collisions, we observe an increase of B_2 with increasing transverse momentum indicating a smaller effective volume in line with our expectation from HBT correlations. In nucleus + nucleus collisions, we observe a) a strong centrality dependence of B_2 in line with expectations, and b) a strong energy dependence of B_2 at fixed centrality, which however levels off towards higher energies. We explain this non-monotonous structure as a volume effect up to $\sqrt{s_{NN}} \approx 20$ GeV, counteracted by strong space-momentum correlations at higher energies, which have been shown to create a plateau in B_2.

Data Availability Statement This manuscript has no associated data or the data will not be deposited. [Authors' comment: The datasets generated during and/or analysed during the current study are available from the corresponding author on reasonable request.]

References

1. J.W. Harris, B. Muller, Ann. Rev. Nucl. Part. Sci. **46**, 71 (1996). arXiv:hep-ph/9602235
2. B. Monreal et al., Phys. Rev. C **60**, 031901 (1999). arXiv:nucl-th/9904080
3. S. Mrowczynski, Production of light nuclei at colliders—coalescence vs. thermal model (2020). arXiv2004.07029
4. J. Schaffner-Bielich, R. Mattiello, H. Sorge, Phys. Rev. Lett. **84**, 4305 (2000). arXiv:nucl-th/9908043
5. Y. Sun, A. Botvina, A. Obertelli, A. Corsi, M. Bleicher, Phys. Rev. C **98**, 024903 (2018). arXiv.1712.04658
6. P. Braun-Munzinger, B. Dnigus, Nucl. Phys. A **987**, 144 (2019). arXiv.1809.04681
7. R. Mattiello, A. Jahns, H. Sorge, H. Stöcker, W. Greiner, Phys. Rev. Lett. **74**, 2180 (1995)
8. J. Nagle, B. Kumar, D. Kusnezov, H. Sorge, R. Mattiello, Phys. Rev. C **53**, 367 (1996)
9. S. Sombun, K. Tomuang, A. Limphirat, P. Hillmann, C. Herold, J. Steinheimer, Y. Yan, M. Bleicher, Phys. Rev. C **99**, 014901 (2019). arXiv.1805.11509
10. K.J. Sun, C.M. Ko, B. Dnigus, Phys. Lett. B **792**, 132 (2019). arXiv.1812.05175
11. K.J. Sun, C.M. Ko (2020). arXiv:2005.00182
12. A. Schwarzschild, C. Zupancic, Phys. Rev. **129**, 854 (1963)
13. H. Gutbrod, A. Sandoval, P. Johansen, A.M. Poskanzer, J. Gosset, W. Meyer, G. Westfall, R. Stock, Phys. Rev. Lett. **37**, 667 (1976)
14. J.I. Kapusta, Phys. Rev. C **21**, 1301 (1980)
15. R. Scheibl, U.W. Heinz, Phys. Rev. C **59**, 1585 (1999). arXiv:nucl-th/9809092
16. Z. Feckov, J. Steinheimer, B. Tomšik, M. Bleicher, Phys. Rev. C **93**, 054906 (2016). arXiv.1603.05854
17. S. Mrowczynski, Phys. Lett. B **308**, 216 (1993)
18. M. Bleicher, C. Spieles, A. Jahns, R. Mattiello, H. Sorge, H. Stöcker, W. Greiner, Phys. Lett. B **361**, 10 (1995). arXiv.nucl-th/9506009
19. S. Bazak, S. Mrowczynski, Mod. Phys. Lett. A **33**, 1850142 (2018). arXiv.1802.08212
20. S. Bass et al., Prog. Part. Nucl. Phys. **41**, 255 (1998). arXiv:nucl-th/9803035
21. M. Bleicher et al., J. Phys. G **25**, 1859 (1999). arXiv:hep-ph/9909407
22. P. Hillmann, J. Steinheimer, T. Reichert, V. Gaebel, M. Bleicher, S. Sombun, C. Herold, A. Limphirat, J. Phys. G **47**, 055101 (2020). arXiv.1907.04571
23. T. Reichert, P. Hillmann, A. Limphirat, C. Herold, M. Bleicher, J. Phys. G **46**, 105107 (2019). arXiv.1903.12032
24. P. Hillmann, J. Steinheimer, M. Bleicher, J. Phys. G **45**, 085101 (2018). arXiv.1802.01951
25. T. Reichert, P. Hillmann, M. Bleicher (2020). arXiv.2004.10539
26. P. Hillmann, J. Steinheimer, T. Reichert, V. Gaebel, M. Bleicher, S. Sombun, C. Herold, A. Limphirat, Astron. Nachr. **340**, 996 (2019)
27. X. Deng, Y. Ma, Phys. Lett. B **808**, 135668 (2020). arXiv.2006.12337
28. D.H. Rischke, S. Bernard, J.A. Maruhn, Nucl. Phys. A **595**, 346 (1995). arXiv:nucl-th/9504018
29. D.H. Rischke, Y. Pursun, J.A. Maruhn, Nucl. Phys. A **595**, 383 (1995), [Erratum: Nucl.Phys.A **596**, 717–717 (1996)]. arXiv:nucl-th/9504021
30. H. Petersen, J. Steinheimer, G. Burau, M. Bleicher, H. Stöcker, Phys. Rev. C **78**, 044901 (2008). arXiv.0806.1695
31. P. Huovinen, H. Petersen, Eur. Phys. J. A **48**, 171 (2012). arXiv.1206.3371
32. J. Steinheimer, K. Gudima, A. Botvina, I. Mishustin, M. Bleicher, H. Stöcker, Phys. Lett. B **714**, 85 (2012). arXiv.1203.2547
33. S. Acharya et al., ALICE. Phys. Rev. C **97**, 024615 (2018). arXiv.1709.08522
34. D. Oliinychenko, L.G. Pang, H. Elfner, V. Koch, Phys. Rev. C **99**, 044907 (2019). arXiv.1809.03071
35. S. Acharya et al. (ALICE), Phys. Lett. B **794**, 50 (2019). arXiv.1902.09290
36. J. Adam et al. (ALICE), Phys. Rev. C **93**, 024917 (2016). arXiv.1506.08951
37. S. Acharya et al. (ALICE), Eur. Phys. J. C **80**, 889 (2020). arXiv.2003.03184

38. H. Liu, D. Zhang, S. He, Kj Sun, N. Yu, X. Luo, Phys. Lett. B **805**, 135452 (2020). arXiv.1909.09304
39. J. Adam et al. (STAR), Phys. Rev. C **99**, 064905 (2019). arXiv.1903.11778
40. P.Z. Skands, Phys. Rev. D **82**, 074018 (2010). arXiv.1005.3457
41. S. Acharya et al. (ALICE), Eur. Phys. J. C **77**, 658 (2017). arXiv.1707.07304
42. S. Akkelin, Y. Sinyukov, Phys. Lett. B **356**, 525 (1995)
43. A. Kittiratpattana, M.F. Wondrak, M. Hamzic, M. Bleicher, C. Herold, A. Limphirat (2020). arXiv.2006.03052